New Insights into Phase-Mechanism Relationship of Mg$_x$MnO$_2$ Nanowires in Aqueous Zinc-Ion Batteries

Zhongzhuo Yang, Xuelei Pan, Yuanhao Shen, Renpeng Chen, Tianzhao Li, Lin Xu,* and Liqiang Mai

In response to the call for safer energy storage systems, rechargeable aqueous manganese-based zinc-ion (Zn-ion) batteries using mild electrolyte have attracted extensive attention. However, the charge-storage mechanism and structure change of manganese-based cathode remain controversial topics. Herein, a systematic study to understand the electrochemical behavior and charge storage mechanism based on a 3 × 3 tunnel-structured Mg$_x$MnO$_2$ as well as the correspondence between different tunnel structures and reaction mechanisms are reported. The energy storage mechanism of the different tunnel structure is surface faradaic dissolution/deposition coupled with an intercalation mechanism of cations in aqueous electrolyte, which is confirmed by in situ X-ray diffraction, in situ Raman and ex situ extended X-ray absorption fine structure. The deposition process at the cathode is partially reversible due to the accumulation of a birnessite layer on the surface. Compared to smaller tunnels, the 3 × 3 tunnel structure is more conducive to deposit new active materials from the electrolyte. Therefore, pristine Mg$_x$MnO$_2$ nanowires with large tunnels display an excellent cycling performance. This work sheds light on the relationship between the tunnel structure and Mn^{2+} deposition and provides a promising cathode material design for aqueous Zn-ion batteries.

1. Introduction

Due to the safety issues and scarcity of lithium (Li) resources, the development of Li-ion battery cannot meet the requirements of environmentally friendly and sustainable energy storage. Aqueous Zn-ion battery is one of the alternative battery systems owing to the low-cost, intrinsic safety, and high ionic conductivity of the aqueous electrolyte.[1–3] A series of high-performance cathode materials, such as Prussian blue analogues,[4] vanadium oxides,[5] and manganese oxides have been widely reported for rechargeable aqueous Zn-ion batteries. Among them, manganese oxides have shown promising potential because of the low price of raw materials, rich oxidation states, and abundant crystal structures.

Unlike the Li-ion battery and sodium-ion (Na-ion) battery that have been extensively discussed, the reported mechanism of aqueous Zn-ion battery is still controversial, especially for the manganese-based system. According to previous reports, manganese oxides as the cathode of aqueous Zn-ion battery always suffer from capacity fading and poor reaction reversibility.[6–8] In this battery system, carriers are not only Zn^{2+}, but also H$^+$ and even Mn^{2+} in the electrolyte. Multiple carriers and multiphase reaction make the mechanism difficult to unify. Several reaction mechanisms have been reported, such as Zn^{2+} intercalation forming spinel ZnMn$_2$O$_4$[9–10] or layered Zn-buserite,[11] H$^+$ intercalation forming MnOOH,[12–15] Zn^{2+}/H$^+$ co-intercalation,[16–17] and dissolution-deposition reaction.[6–7] Meanwhile, the method that pre-adding Mn^{2+} to electrolyte inhibits the dissolution of the cathode has been proposed, which would improve cycling and rate performance. But the solubility of manganese oxides in mild aqueous is nearly negligible and Mn^{2+} may be electrodeposited to the surface of electrode,[8,14,18] which means that adding Mn^{2+} to improve performance probably has other interpretations. It is these pending issues that need to be further explored.

As is well known, polymorphs of manganese oxides are composed of [MnO$_6$] octahedra which are shared by corners or edges to form different phases with various tunnel or layered structures.[8] Researches on the mechanism are usually based on a certain phase up to now. However, there is rare analysis on whether the phases with similar crystal structures have similar or identical mechanisms. For example, in the previous work, different phases of manganese oxides (α and β) exhibit the same cyclic voltammetry (CV) curve, but the explanation of their mechanism is completely different.[11,19] The correspondence between the mechanism and similar crystal structure has not been revealed, such as different tunnel sizes (3 × 3 tunnels in Mg$_x$MnO$_2$ and 2 × 2 tunnels in K$_x$MnO$_2$) or different interlayer spacing (birnessite, buserite, and vernadite). Therefore, a universal mechanism is urgently needed to explain the

Z. Yang, X. Pan, Y. Shen, R. Chen, T. Li, L. Xu, L. Mai
State Key Laboratory of Advanced Technology for Materials Synthesis and Processing
School of Materials Science and Engineering
Wuhan University of Technology
Wuhan 430070, China
E-mail: linxu@whut.edu.cn
L. Xu, L. Mai
Foshan Xianhu Laboratory of the Advanced Energy Science and Technology Guangdong Laboratory
Xianhu hydrogen Valley
Foshan 528200, China

similarities and differences among similar crystal structures in the reaction process.

In this regard, we systematically and comprehensively reveal the relationship between the tunnel structure of manganesed-based cathodes and the reaction mechanism in Zn-ion batteries. This relationship was disclosed by probing the electrochemical behavior and structure evolution of Mg_xMnO_2 with 3×3 tunnel and K_xMnO_2 with 2×2 tunnel. This work displays a Zn^{2+} insertion and Mn^{2+} deposition reaction mechanism in Mg_xMnO_2 with 3×3 tunnel structure. Mg_xMnO_2 stabilized by magnesium ions is easier to induce deposition upon cycling and the deposited product is layered structure. Therefore, Mg_xMnO_2 exhibits better cycling performance and rate performance compared to K_xMnO_2. In addition, the in-depth insights into the relationship between tunnel structure and reaction mechanism could provide a guidance in Li/Na/Mg-ion battery system.

2. Results and Discussion

The tunnel-structured Mg_xMnO_2 and K_xMnO_2 nanowires were synthesized by using hydrothermal methods (described in Experimental Section). The as-obtained Mg_xMnO_2 and K_xMnO_2 cathode materials were first characterized with powder X-ray diffraction (XRD), X-ray photoelectron spectroscopy (XPS), and Raman spectroscopy to investigate the crystal structure and chemical composition. The phase of the samples was examined by XRD in **Figure 1**a. All the diffraction peaks are indexed to monoclinic Mg_xMnO_2 (todorokite, JCPDS PDF #38-475, space group: $P2/m$) and tetragonal K_xMnO_2 (hollandite, JCPDS PDF #44-0141, space group: $I4/m$). Raman spectra are displayed in Figure 1b and Figure S1 (Supporting Information). Within many kinds of manganese oxides, Mn and O atoms are coordinated in $[MnO_6]$ octahedra. In Figure 1b, the ν_1 band (located at ≈ 640 cm^{-1}) belongs to the symmetric stretching vibration of the Mn–O bond in the $[MnO_6]$ octahedra, which is perpendicular to the direction of $[MnO_6]$ octahedra chains and decided by the type of ion in the tunnels. The ν_2 (located at ≈ 580 cm^{-1}) belongs to the Mn–O vibration along the chains of the framework. The ν_3 band located at ≈ 180 cm^{-1} in the low-frequency assigned to an external vibration that derives from the translational motion of the $[MnO_6]$ octahedra, which is also affected by the tunnel ion.[20] The Raman spectra suggest that the Mg_xMnO_2 and K_xMnO_2 belong to todorokite and hollandite, respectively.[21–22] The XPS was used to characterize the chemical compositions and states of the two samples. The XPS spectra confirmed that Mg_xMnO_2 contains Mn, O, Mg elements and Mn, O, K elements are involved in K_xMnO_2 (Figure 1c and Figure S2: Supporting Information).

In general, tunnel-structured manganese oxides synthesized by hydrothermal process always exhibit 1D morphology, such as nanowires and nanorods. As expected, both of Mg_xMnO_2 and K_xMnO_2 exhibit nanowire morphology as shown in transmission electron microscope (TEM) images (Figure 1d,e). The average diameter of the Mg_xMnO_2 nanowire is ≈ 30 nm. Besides, the well-resolved lattice fringes with an interplanar distance of 9.7 Å which is exactly $\sqrt{2}$ times length of the tunnel structure diagonal, can be assigned to the (100) plane of the
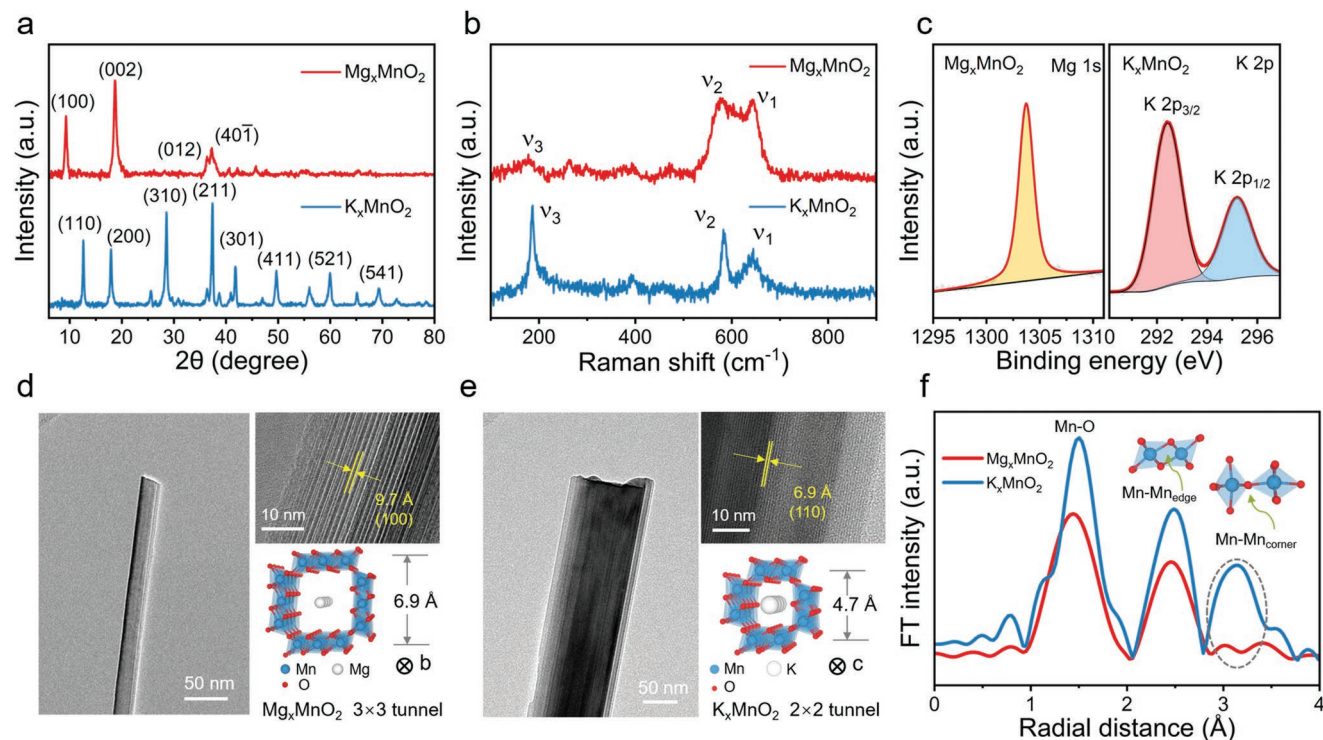
Figure 1. Structure characterizations of as-prepared Mg_xMnO_2 nanowires. a) XRD patterns, b) Raman spectra, c) High-resolution XPS scans in the Mg 1s and K 2p regions, of Mg_xMnO_2 and K_xMnO_2. TEM images, HRTEM images and crystal structure models of d) Mg_xMnO_2 and e) K_xMnO_2. f) Corresponding Mn K-edge EXAFS spectra of Mg_xMnO_2 and K_xMnO_2.

Mg_xMnO_2 phase. In addition, the Mg_xMnO_2 nanowires are preferentially growing along the [010] direction.[23] With regard to K_xMnO_2, the cross-sectional dimension and the length of nanowires are larger than those of Mg_xMnO_2. The high-resolution transmission electron microscope (HRTEM) images of an individual nanowire display that the d-spacing of lattice fringes at about 6.9 Å refers to the (110) plane of K_xMnO_2 crystal, and the nanowire growing along [001] direction. Different from Mg_xMnO_2 (with the size of ≈6.9 Å × 6.9 Å) constituted by triple chains of edge-sharing $[MnO_6]$ octahedra, K_xMnO_2 only has 2 × 2 tunnels with the size of ≈4.7 Å × 4.7 Å.[24] Besides, energy dispersive spectrometer (EDS) mapping images demonstrate the uniform distribution of elements in the nanowires (Figure S3, Supporting Information).

The local chemical environment of Mn atoms was measured by extended X-ray absorption fine structure (EXAFS) which has been proved effective to analyze manganese oxides.[25–26] It is worth noting that some differences are remarkable, such as the peaks at ≈3 Å, suggesting that Mn atom in Mg_xMnO_2 has different chemical structure with K_xMnO_2 (Figure 1f). The peak at ≈1.5 Å is assigned to the closest Mn–O coordination in the $[MnO_6]$ octahedra. Besides, the peaks located at 2.5 and 3 Å belong to the edge-sharing (Mn-Mn$_{edge}$) and corner-sharing (Mn-Mn$_{corner}$) $[MnO_6]$ octahedra, respectively. The relatively weaker Mn-Mn$_{corner}$ peak in Mg_xMnO_2 means less corner-sharing $[MnO_6]$ octahedra and larger tunnel size in the structure (Figure S4, Supporting Information). The EXAFS strongly confirms again that Mg_xMnO_2 has a larger tunnel size than K_xMnO_2. To sum and note, the differences between the two phases of manganese oxides are mainly concentrated on the tunnel structure and ions that stabilize the tunnel structure (Mg^{2+} in Mg_xMnO_2 and K^+ in K_xMnO_2).

To focus on the electrochemical behavior of different tunnels (Mg_xMnO_2 and K_xMnO_2), we fabricated Zn/Mg_xMnO_2 and Zn/K_xMnO_2 cells with 2 M $ZnSO_4$ + 0.2 M $MnSO_4$ as electrolyte. We performed the CV and galvanostatic charge-discharge (GCD) measurements for both cathodes. **Figure 2**a shows the CV curves of the Mg_xMnO_2 electrode at the first five cycles, which reveals that two pairs of redox peaks are observed at 1.27 V/1.39 V and 1.55 V/1.59 V. As the number of cycles increases, the intensity of two pairs of redox peaks increases significantly. The curves (inset of Figure 2a) further reveal that the peak current of O1 increases from 0.17 to 0.49 mA after 5 cycles while the peak current of O2 changes slightly. In other words, the increase of oxidation peaks mainly concentrates on 1.59 V (O1). However, for K_xMnO_2, the increase of peak at 1.59 V in CV curves is not so obvious as Mg_xMnO_2 (shown in the curve inset of Figure 2b). According to the similar results from Zn/K_xMnO_2 battery in this test system, we hypothesize that the reaction mechanism is shared by the tunnel-structured manganese oxides and the oxidation reaction at high potential (1.59 V) is more pronounced for the large tunnel structure. We then tested GCD measurements at a current density of 100 mA g^{-1} for Mg_xMnO_2 and K_xMnO_2. Two discharge plateaus are observed corresponding to the two reduction peaks in CV curves (Figure S5a,b: Supporting Information). The ultralong capacity-increase process (75 mAh g^{-1} at initial and 370 mAh g^{-1} after 130 cycles) of Mg_xMnO_2 far exceeds the time required for activation in the common battery system, indicating that there is another reaction that provides additional capacity
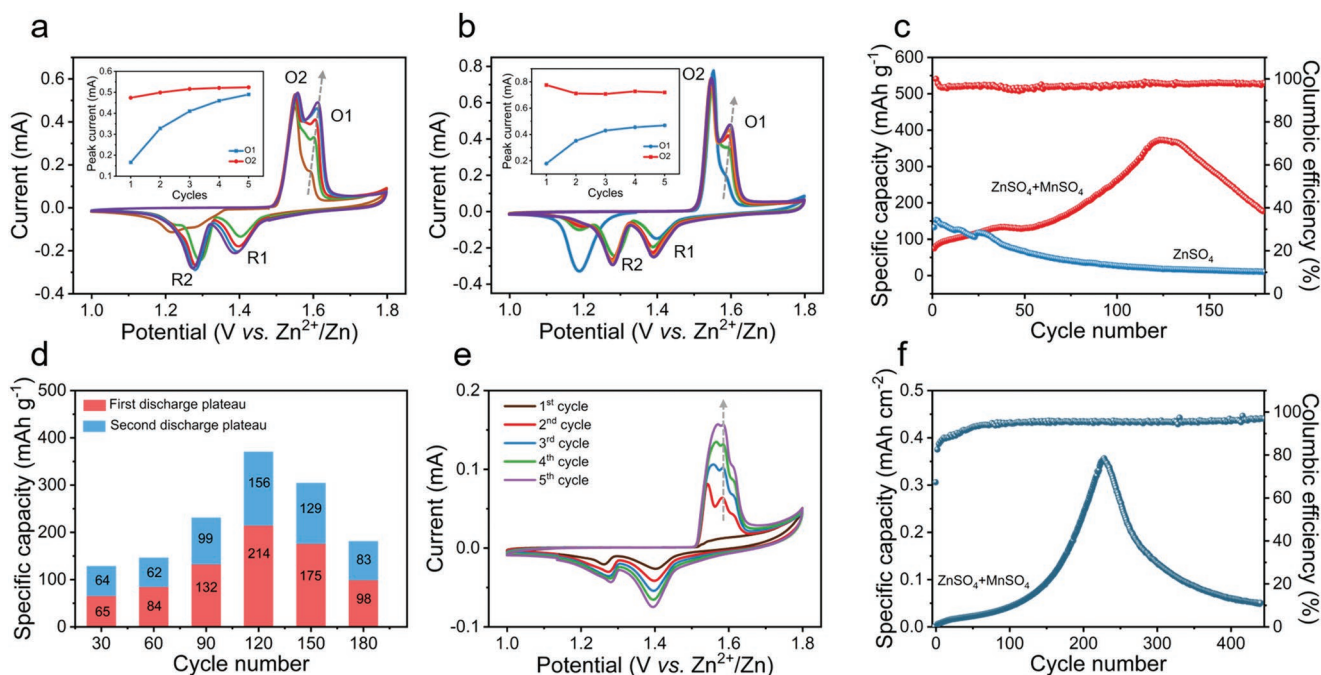
Figure 2. Electrochemical characterizations of Mg_xMnO_2 nanowires. CV curves (inset showing the correspondence between peak currents and number of cycles) of a) Mg_xMnO_2 and b) K_xMnO_2 with 2 M $ZnSO_4$ + 0.2 M $MnSO_4$ electrolyte recorded at a scan rate of 0.1 mV s^{-1} from 1.0 to 1.8 V. c) Cycling performance at 100 mA g^{-1} of Mg_xMnO_2 with 2 M $ZnSO_4$ + 0.2 M $MnSO_4$ electrolyte (red line) and 2 M $ZnSO_4$ electrolyte (blue line). d) Quantitative first and second plateau contribution to capacity delivery in different cycles of Mg_xMnO_2. e) CV curves of carbon paper employing 2 M $ZnSO_4$ + 0.2 M $MnSO_4$ electrolyte recorded at a scan rate of 0.1 mV s^{-1}. f) Cycling performance at 100 mA cm^{-1} of carbon paper with 2 M $ZnSO_4$ + 0.2 M $MnSO_4$ electrolyte.
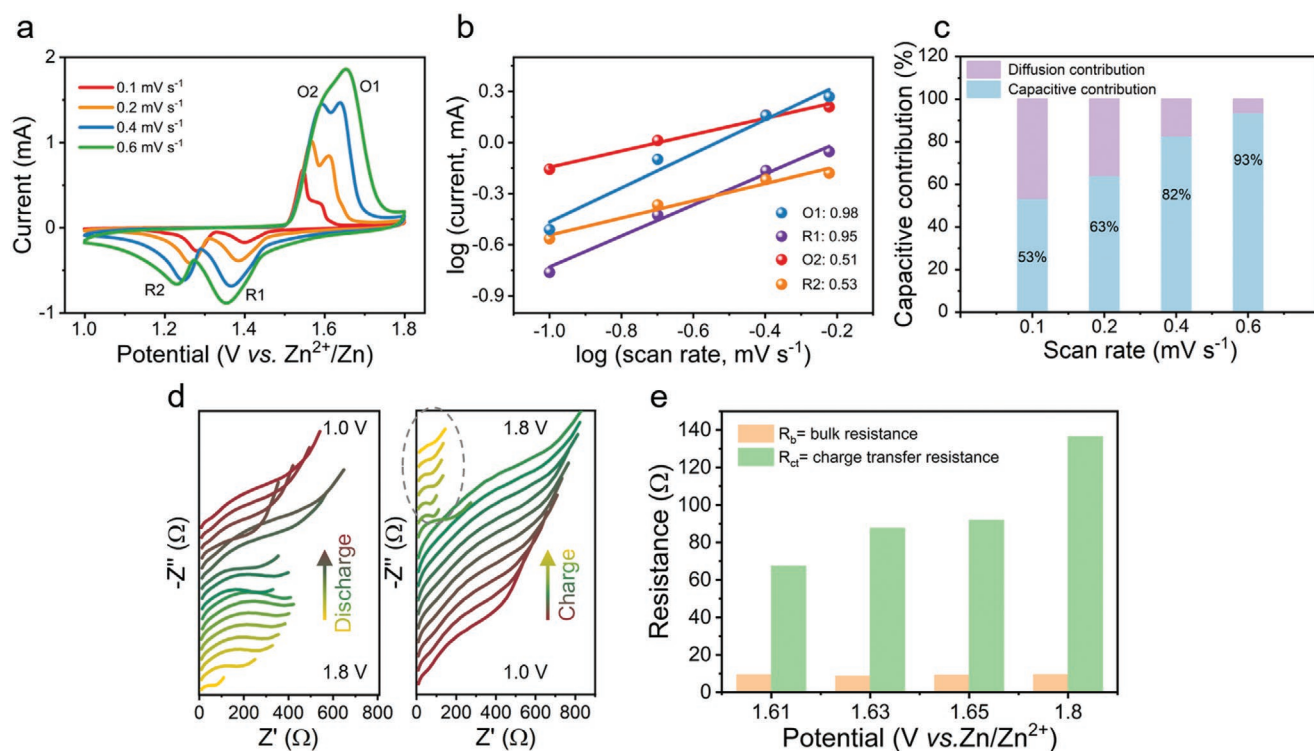
Figure 3. Kinetics analyses of the electrochemical reactions in Mg_xMnO_2 nanowires. a) CV curves of Mg_xMnO_2 at the sweep rates ranging from 0.1 to 0.6 mV s⁻¹. b) Log (i) versus log (v) plots at different oxidation and reduction states based on CV curves. c) The ratio of capacitive contribution at different scan rates of Mg_xMnO_2. d) SPEIS plots of Mg_xMnO_2 during discharge/charge process. e) Fitted EIS component values of Mg_xMnO_2 at the selected potential from the dashed cycle (charge 1.61 V, charge 1.63 V, charge 1.65 V, charge 1.8 V).

(Figure 2c).[27] The capacity statistics further demonstrate that the growth of capacity mainly comes from the first discharge plateau (an increase from 65 to 214 mAh g⁻¹) while the second discharge plateau only exhibits small changes compared to the first one (Figure 2d). It is rational to conclude that the capacity-attenuation (begins from 130th cycles) mainly comes from the inferior reactivity of the reaction at the first discharge plateau. However, the capacity growth of K_xMnO_2 is limited, and is only provided by the first plateau. The capacity-increase process of K_xMnO_2 is only about 60 cycles, far less than the Mg_xMnO_2, indicating the large tunnel structure is more susceptible to this reaction (Figure S5c,d: Supporting Information).

After the above comparison, we consider whether the redox characteristics of the reaction at 1.59 V/1.39 V (O1/R1) do not depend on the electrode material. Therefore, we set up the carbon paper cathode as the blank control group. As we expected, due to the lack of active materials, the capacity is close to zero in the first cycle (Figure S6a, Supporting Information). Subsequently, two pairs of redox peaks gradually appear, indicating that a new redox reaction appeared on carbon paper (Figure 2e and Figure S6b: Supporting Information). It is worth noting that its capacity rapidly increases in 250 cycles and then decreases promptly during cycling (Figure 2f), which is similar to the GCD curve of Mg_xMnO_2. We further analyzed Raman spectra, optical image, SEM image, EDS image of carbon paper after 250 cycles (Figure S7, Supporting Information). Even if there are no cathode materials, the deposited layer will also emerge during cycling. However, the capacity does not always

increase, and there is a rapid decay after reaching a certain point. The detailed reaction mechanism will be discussed later. There is a consensus that adding Mn^{2+} to the electrolyte is a conventional method to improve the performance of manganese-based Zn-ion battery.[28–29] Therefore, we explored whether the presence of Mn^{2+} in the solution has an effect on the reaction we proposed above by CV (Figure S8, Supporting Information) and GCD measurements (Figure 2c). For both cathodes, the capacity decreases rapidly at the beginning. Therefore, this additional reaction mainly occurs in $ZnSO_4$ + $MnSO_4$ electrolyte associated with Mn^{2+} in the electrolyte. In general, the characteristics of redox reaction in the capacity-increase process do not depend on the electrode materials, but they are affected by the tunnel structure of the electrode and the composition of the electrolyte. The reaction extent can be regulated by different phases with the unchanged redox characteristics.

To evidence this inference, we analyzed the kinetics behaviors of two pairs of redox reaction in Mg_xMnO_2 by CV measurement at different scan rates (**Figure 3**a). Based on the previous work,[30] the relationship between scan rates (v) and currents (i) is described in Equation (1) where a and b are adjustable parameters. In the meantime, b value is the slope of the linear relationship between log i and log v, which is identified to distinguish the charge storage types as described in Equation (2).

$$i = av^b \tag{1}$$

$$\log i = b \log v + \log a \tag{2}$$

Generally, when b value is approaching to 1, it is suggested to be a capacitive-controlled behavior. When b is close to 0.5, it indicates a diffusion-controlled behavior. For Mg_xMnO_2, the b value of the R1/O1 peak is 0.95/0.98 (Figure 3b), which is larger than that of K_xMnO_2 in Figure S9 (Supporting Information), suggesting that Mg_xMnO_2 exhibits the faster interfacial reaction kinetics for the redox reaction at high potential, consistent with the surface deposition reaction mentioned previously. Meanwhile, the b value of the R2/O2 peaks is 0.53/0.51, approaching 0.5, which means the kinetics behavior is mainly controlled by diffusion at low potential. It is demonstrated that the kinetics of the reaction can also be regulated by phase-engineering. Besides, Dunn and co-workers provide a method to obtain capacitive contribution proportion. [31–32] The total current $i(v)$ could be divided into capacitive (k_1v) and diffusion controlled ($k_2v^{1/2}$) current responses as calculated by Equation (3).

$$i(v) = k_1 v + k_2 v^{1/2} \tag{3}$$

As shown in Figure 3d, the capacity contribution of Mg_xMnO_2 is 52.7% at 0.1 mV s^{-1}, and gradually increases to 93% at 1 mV s^{-1}, proving the high surface reactivity (Figure S10, Supporting Information).

To further understand the reaction process and the deposition behavior of the cathode exactly, staircase potential electrochemical impedance spectroscopy (SPEIS) measurements were performed. As displayed in Figure 3d, the resistance plots vary with the potential change. In the discharge process (Figure 3d left, from 1.8 to 1.0 V), the cell first exhibits a single semicircle which corresponds to the charge transfer resistance, and the impedance shows a straight Warburg line nearly 45°, indicating fast solid-state diffusion. Then the cell at 1.8 V shows two semicircles with a large increase of impedance, which can be explained by the formation of a new phase. In the charge process, the impedance decreases until 1.59 V approximately showing nearly opposite tendency to discharge as expected. The selected potentials of the Nyquist impedance are shown in Figure S11 (Supporting Information). From 1.59 to 1.8 V, corresponding to manganese oxide deposition process, the resistance increases again, which indicates the deposition layer has a poor conductivity (fitting results shown in Figure 3e). Therefore, due to the appearance of the deposition layer, the conductivity of cathode gradually deteriorates which leads to capacity decrease.

In order to in situ monitor the structural change during cycling and analyze the mechanism of capacity increase and decay, we conducted the in situ XRD measurement on Mg_xMnO_2 (**Figure 4**a). The diffraction peaks of the Mg_xMnO_2 always remain unchanged during the charge and discharge process. The emerging of new diffraction peaks (red arrows) is observed during the discharge process. The new peaks are well indexed to $Zn_4SO_4(OH)_6 \cdot 5H_2O$ (JCPDS PDF #039-0688)
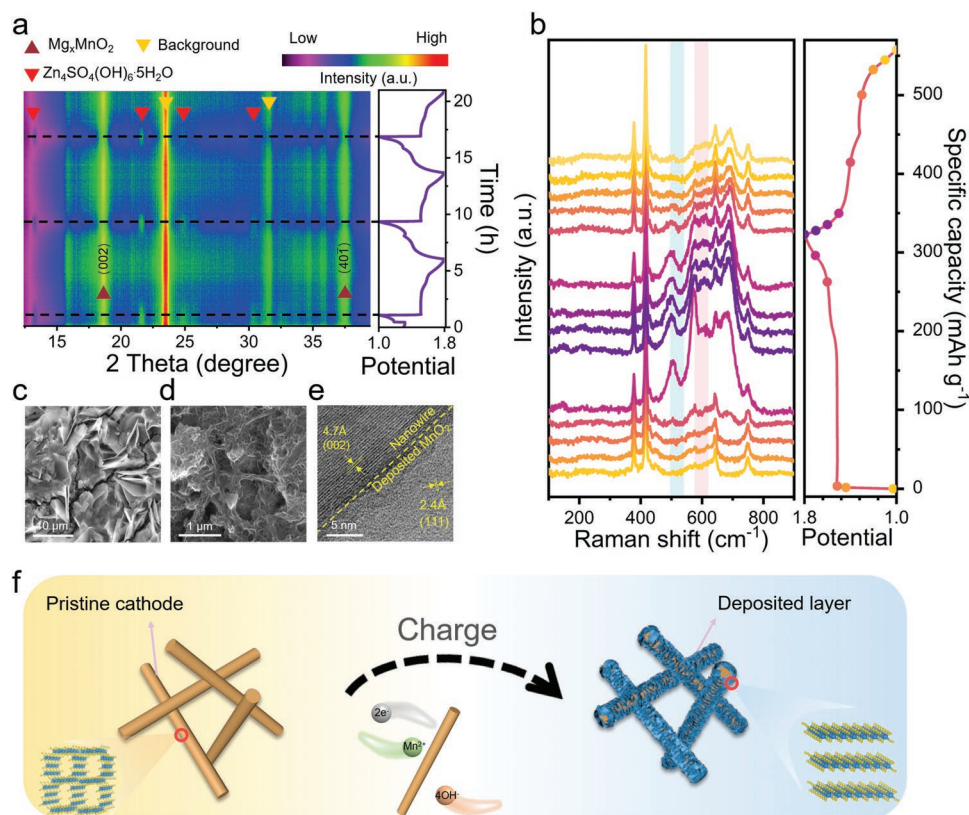
Figure 4. In situ characterizations of surface faradaic dissolution/deposition and intercalation mechanism. a) In situ XRD patterns of Mg_xMnO_2 during the first three cycles at 100 mA g^{-1} and the corresponding charge-discharge curves. b) In situ Raman spectra of Mg_xMnO_2 at 100 mA g^{-1} and the corresponding charge-discharge curves. c) SEM image at fully discharged state of Mg_xMnO_2. d) SEM image and e) HRTEM image of Mg_xMnO_2 at fully charged state. f) Charge storage mechanism illustration of Zn-Mg_xMnO_2 during charge process.

ADVANCED
SCIENCE NEWS
www.advancedsciencenews.com

NANO · MICRO
small
www.small-journal.com

which disappear during the charge process. The appearance of $Zn_4SO_4(OH)_6 \cdot 5H_2O$ means that H^+ participates in the reaction, which changes the pH value of the system. Consistent with the result of in situ XRD, SEM image further confirms the appearance of $Zn_4SO_4(OH)_6 \cdot 5H_2O$ in Figure 4c. Contrary to the previous experimental observations, it is difficult to observe the formation of the new phase of manganese oxides in multiple charge processes, because its crystallinity is too poor and the diffraction peaks are not strong enough to be distinguished in a lab-scaled X-ray diffractometer.

To solve the problem that the change in the charge process is difficult to be observed in detail by in situ XRD, we collected in situ Raman spectra of Mg_xMnO_2 in Figure 4b. Raman spectra are sensitive to the nature of molecular and crystal structures, especially for polymorphous manganese oxides. In order to clearly show the appearance and disappearance of charge products, we selected a part which was charged first and then discharged. Meanwhile, the complete in situ Raman spectra were placed in Figure S12 (Supporting Information) to show the reversibility of Mg_xMnO_2. Initially, all the Raman bands are consistent well with Mg_xMnO_2, and no new peaks emerge at the first lower charge plateau. When charging to the second plateau (around 1.59 V), it gives rise to a series of new peaks which disappear at the first discharge plateau subsequently. These new peaks indicate the formation of charge-state product. The Raman bands located at ≈503 and ≈575 cm^{-1} are the typical features of layered-manganese oxides family,[33–34] which demonstrate that the charge-state

product should be layered-structure manganese oxide. Contrary to the previous reports, the discharge products such as MnOOH and Mn_3O_4,[10,12] which others thought exist in the cycling process, do not appear in in situ Raman of Mg_xMnO_2. Moreover, the above-mentioned spectral features can also be observed in K_xMnO_2 (Figure S13, Supporting Information). Meanwhile, the corresponding SEM image of Mg_xMnO_2 at fully charge state shows that a large amount of nanosheets in nanometer range, appears on the surface of the electrode (Figure 4d). As shown in Figure 4e and Figure S14 (Supporting Information), the HRTEM and TEM images show that Mg_xMnO_2 nanowire remain its crystal structure and morphology after cycling. In the obvious deposition layer, the lattice fringes with an interplanar distance of 2.4 Å can be assigned to ($\bar{1}11$) plane of manganese oxide in δ-phase (birnessite, JCPDS PDF #080-1098).

In a word, in situ characterization monitors the charge and discharge process in real-time. Raman illustrates the amorphous birnessite as product of the charge process (schematic illustration in Figure 4f), and XRD presents the products $Zn_4SO_4(OH)_6 \cdot 5H_2O$ of the discharge process in a reversible manner. Combined with in situ experimental data, there are two possible reasons why it is easier to induce deposition: a) "Quasi-Epitaxial Growth": The similar structure makes the Mg_xMnO_2 easier to electrodeposit layered-manganese oxides on the surface. b) The large tunnel structure and the water molecules in Mg_xMnO_2 are conducive to the infiltration of the aqueous electrolyte (Figure S15, Supporting Information).
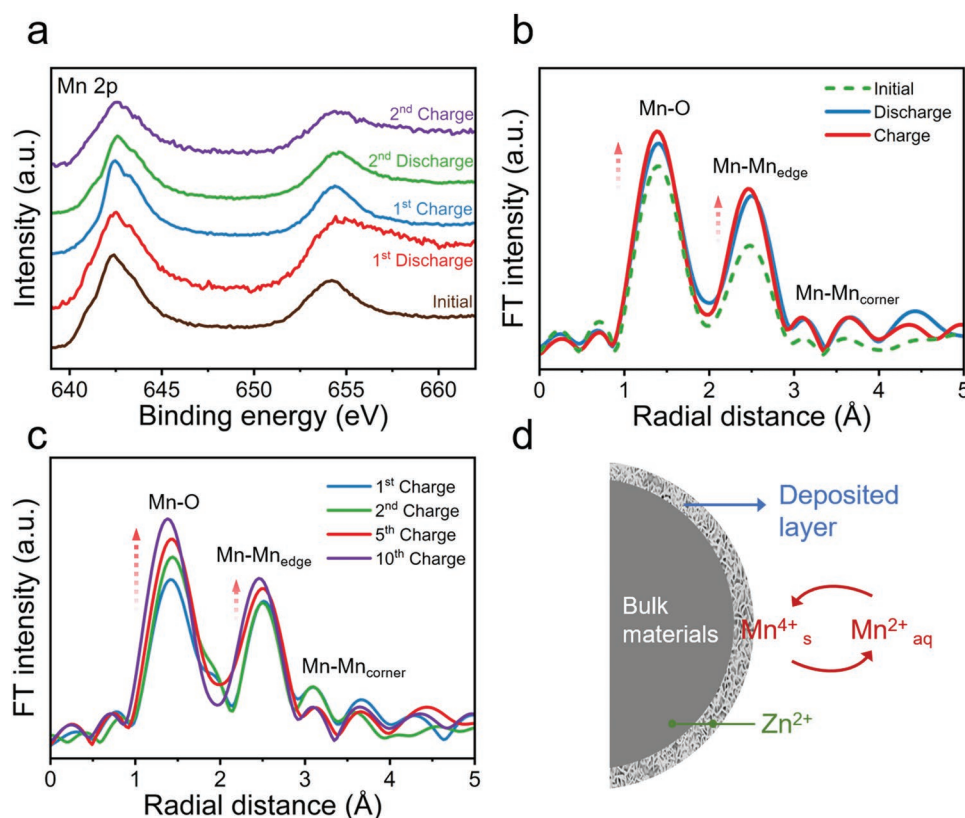
Figure 5. Electronic structure evolution of Mg_xMnO_2 nanowires. a) High-resolution Mn 2p XPS spectra at different states. b) EXAFS spectra of Mg_xMnO_2 at different charge/discharge states. c) EXAFS spectra of Mg_xMnO_2 at fully charge states in different cycles. d) Schematic diagram of battery capacity-decay mechanism.

To gain in-depth understanding of oxidation state and electronic structure changes, ex situ XPS scans and EXAFS spectra were collected at selected state. The mean Mn valence remains almost unchanged during cycling (**Figure 5**a). Combined with the discussion above, there exists both one-electron charge transfer reaction and two-electron transfer reaction: a) one-electron charge transfer reaction: $Mn^{4+}_s + e^- \rightarrow Mn^{3+}_s \rightarrow Mn^{4+}_s + Mn^{2+}_{aq}$.[35] and b) two-electron charge transfer reaction: $Mn^{4+}_s + 2e^- \rightarrow Mn^{2+}_{aq}$. The phase uncorrected Fourier transform (FT) (k^3-weighted) of the selected Mn K-edge EXAFS at the pristine, charge and discharge states are shown in Figure 5b. When the electrode was fully charged, the peaks corresponding to Mn-Mn$_{corner}$ reveals small variation in peak shift and intensity variations compared to the discharge state, while the increase of intensity is obvious for the Mn-O and Mn-Mn$_{edge}$ peak. This result is indicative that the deposition production is the layered-manganese oxides in δ-phase which is lack corner-shared [MnO$_6$] octahedra.[36] However, this deposition reaction is incomplete reversible. As we expected, during cycling, the amplitude of FT peaks of Mn-O and Mn-Mn$_{edge}$ gradually increased, which does not fully recover after times of charging, even in the presence of partial dissolution (Figure 5c). It is worth noting that the increase concentrates on signals of Mn-O and Mn-Mn$_{edge}$, which strongly demonstrate that accumulation of manganese oxide is layer structure again. Nevertheless, as the result of SPEIS demonstrated, the conductivity of layered-manganese oxide is relatively poor. A large number of materials with poor conductivity covered on the surface of the electrode weaken its electrochemical activity, resulting in capacity degradation (Figure 5d). Notably, EXAFS spectra of K$_x$MnO$_2$ electrode demonstrate similar behavior with that of Mg$_x$MnO$_2$, suggesting the common electrode reaction mechanism among different tunnel manganese oxide polymorphs again (Figure S16, Supporting Information).

3. Conclusion

In summary, we synthesized Mg$_x$MnO$_2$ and K$_x$MnO$_2$ nanowires as cathodes for aqueous Zn-ion battery to reveal the relationship between tunnel structure and reaction mechanism during cycling. It is found that the characteristics of redox reaction in the capacity-increase process are affected by the tunnel structure of the electrode. Mg$_x$MnO$_2$ with 3×3 tunnel exhibits the faster deposition reaction kinetics than K$_x$MnO$_2$ and tends to deposit more manganese oxide in charge process. Combined with SPEIS, in situ Raman, in situ XRD and EXAFS analysis, the charge-state product is layered manganese dioxide with poor conductivity. Beyond that, the capacity decay mainly comes from the gradual deterioration of the conductivity of the cathode. We prove that with the unchanged redox characteristics, the reaction kinetics/extent can be regulated by phase-engineering, which has a great significance and can guide future research in aqueous Zn-ion battery.

Supporting Information

Supporting Information is available from the Wiley Online Library or from the author.

Conflict of Interest

The authors declare no conflict of interest.

Data Availability Statement

The data that support the findings of this study are available from the corresponding author upon reasonable request.

[1] C. Yang, J. Chen, X. Ji, T. P. Pollard, X. Lü, C. Sun, S. Hou, Q. Liu, C. Liu, T. Qing, Y. Wang, O. Borodin, Y. Ren, K. Xu, C. Wang, *Nature* **2019**, *569*, 245.

[2] J. Zheng, Q. Zhao, T. Tang, J. Yin, D. Quilty Calvin, D. Renderos Genesis, X. Liu, Y. Deng, L. Wang, C. Bock David, C. Jaye, D. Zhang, S. Takeuchi Esther, J. Takeuchi Kenneth, C. Marschilok Amy, A. Archer Lynden, *Science* **2019**, *366*, 645.

[3] Y. Zhang, F. Wan, S. Huang, S. Wang, Z. Niu, J. Chen, *Nat. Commun.* **2020**, *11*, 2199.

[4] L. Ma, S. Chen, C. Long, X. Li, Y. Zhao, Z. Liu, Z. Huang, B. Dong, J. A. Zapien, C. Zhi, *Adv. Energy Mater.* **2019**, *9*, 1902446.

[5] D. Kundu, B. D. Adams, V. Duffort, S. H. Vajargah, L. F. Nazar, *Nat. Energy* **2016**, *1*, 16119.

[6] Y. Liu, J. Zhi, M. Sedighi, M. Han, Q. Shi, Y. Wu, P. Chen, *Adv. Energy Mater.* **2020**, *10*, 2002578.

[7] Y. Ma, Y. Ma, T. Diemant, K. Cao, X. Liu, U. Kaiser, R. J. Behm, A. Varzi, S. Passerini, *Adv. Energy Mater.* **2021**, *11*, 2100962.

[8] M. Song, H. Tan, D. Chao, H. J. Fan, *Adv. Funct. Mater.* **2018**, *28*, 1802564.

[9] Q. Zhao, X. Chen, Z. Wang, L. Yang, R. Qin, J. Yang, Y. Song, S. Ding, M. Weng, W. Huang, J. Liu, W. Zhao, G. Qian, K. Yang, Y. Cui, H. Chen, F. Pan, *Small* **2019**, *15*, 1904545.

[10] M. Liu, Q. Zhao, H. Liu, J. Yang, X. Chen, L. Yang, Y. Cui, W. Huang, W. Zhao, A. Song, Y. Wang, S. Ding, Y. Song, G. Qian, H. Chen, F. Pan, *Nano Energy* **2019**, *64*, 103942.

[11] N. Zhang, F. Cheng, J. Liu, L. Wang, X. Long, X. Liu, F. Li, J. Chen, *Nat. Commun.* **2017**, *8*, 405.

[12] J. Wang, J. Wang, H. Liu, Z. You, Z. Li, F. Kang, B. Wei, *Adv. Funct. Mater.* **2021**, *31*, 2007397.

[13] Y. Jin, L. Zou, L. Liu, M. H. Engelhard, R. L. Patel, Z. Nie, K. S. Han, Y. Shao, C. Wang, J. Zhu, H. Pan, J. Liu, *Adv. Mater.* **2019**, *31*, 1900567.

[14] H. Moon, K. Ha, Y. Park, J. Lee, M. Kwon, J. Lim, M. Lee, D. Kim, J. H. Choi, J. Choi, K. T. Lee, *Adv. Sci.* **2021**, *8*, 2003714.

[15] Q. Liu, Z. Hao, X. Liao, X. Pan, S. Li, L. Xu, L. Mai, *Small* **2019**, *15*, 1902141.

[16] J. Huang, Z. Wang, M. Hou, X. Dong, Y. Liu, Y. Wang, Y. Xia, *Nat. Commun.* **2018**, *9*, 2906.

[17] L. E. Blanc, D. Kundu, L. F. Nazar, *Joule* **2020**, *4*, 771.

[18] X. Zeng, J. Liu, J. Mao, J. Hao, Z. Wang, S. Zhou, C. D. Ling, Z. Guo, *Adv. Energy Mater.* **2020**, *10*, 1904163.

[19] X. Gao, H. Wu, W. Li, Y. Tian, Y. Zhang, H. Wu, L. Yang, G. Zou, H. Hou, X. Ji, *Small* **2020**, *16*, 1905842.

[20] C. Julien, M. Massot, R. BaddourHadjean, S. Franger, S. Bach, J. P. PereiraRamos, *Solid State Ionics* **2003**, *159*, 345.

[21] H. Kim, P. C. Stair, *J. Phys. Chem. B* **2004**, *108*, 17019.

[22] J. E. Post, D. A. McKeown, P. J. Heaney, *Am. Mineral.* **2020**, *105*, 1175.

[23] Y. Yuan, C. Liu, B. W. Byles, W. Yao, B. Song, M. Cheng, Z. Huang, K. Amine, E. Pomerantseva, R. ShahbazianYassar, J. Lu, *Joule* **2019**, *3*, 471.

[24] X. Hu, D. A. Kitchaev, L. Wu, B. Zhang, Q. Meng, A. S. Poyraz, A. C. Marschilok, E. S. Takeuchi, K. J. Takeuchi, G. Ceder, Y. Zhu, *J. Am. Chem. Soc.* **2018**, *140*, 6961.

[25] J. Lu, C. Zhan, T. Wu, J. Wen, Y. Lei, A. J. Kropf, H. Wu, D. J. Miller, J. W. Elam, Y.-K. Sun, X. Qiu, K. Amine, *Nat. Commun.* **2014**, *5*, 5693.

[26] R. Zhang, X. Yu, K. Nam, C. Ling, T. S. Arthur, W. Song, A. M. Knapp, S. N. Ehrlich, X. Yang, M. Matsui, *Electrochem. Commun.* **2012**, *23*, 110.

[27] M. H. Alfaruqi, V. Mathew, J. Gim, S. Kim, J. Song, J. P. Baboo, S. H. Choi, J. Kim, *Chem. Mater.* **2015**, *27*, 3609.

[28] D. Wu, L. M. Housel, S. J. Kim, N. Sadique, C. D. Quilty, L. Wu, R. Tappero, S. L. Nicholas, S. Ehrlich, Y. Zhu, A. C. Marschilok, E. S. Takeuchi, D. C. Bock, K. J. Takeuchi, *Energy Environ. Sci.* **2020**, *13*, 4322.

[29] H. Pan, Y. Shao, P. Yan, Y. Cheng, K. S. Han, Z. Nie, C. Wang, J. Yang, X. Li, P. Bhattacharya, K. T. Mueller, J. Liu, *Nat. Energy* **2016**, *1*, 16039.

[30] H. Lindström, S. Södergren, A. Solbrand, H. Rensmo, J. Hjelm, A. Hagfeldt, S. Lindquist, *J. Phys. Chem. B* **1997**, *101*, 7717.

[31] J. Wang, J. Polleux, J. Lim, B. Dunn, *J. Phys. Chem. C* **2007**, *111*, 14925.

[32] T. Brezesinski, J. Wang, S. H. Tolbert, B. Dunn, *Nat. Mater.* **2010**, *9*, 146.

[33] L. Yang, S. Cheng, J. Wang, X. Ji, Y. Jiang, M. Yao, P. Wu, M. Wang, J. Zhou, M. Liu, *Nano Energy* **2016**, *30*, 293.

[34] D. Chen, D. Ding, X. Li, G. H. Waller, X. Xiong, M. A. ElSayed, M. Liu, *Chem. Mater.* **2015**, *27*, 6608.

[35] L. Dai, Y. Wang, L. Sun, Y. Ding, Y. Yao, L. Yao, N. E. Drewett, W. Zhang, J. Tang, W. Zheng, *Adv. Sci.* **2021**, *8*, 2004995.

[36] K. W. Nam, H. Kim, J. H. Choi, J. W. Choi, *Energy Environ. Sci.* **2019**, *12*, 1999.